Finite Elements in Analysis and Design 130 (2017) 27–38

Contents lists available at ScienceDirect

Finite Elements in Analysis and Design

journal homepage: www.elsevier.com/locate/finel

2D and 3D Abaqus implementation of a robust staggered phase-field solution for modeling brittle fracture

Gergely Molnár*, Anthony Gravouil

Laboratoire de Mécanique des Contacts et des Structures, Institut National des Sciences Appliquées de Lyon 18-20, rue des Sciences, 69621 Villeurbanne Cedex, France

ARTICLE INFO

Keywords:
Brittle fracture
Crack propagation
Abaqus UEL
Phase-field
Staggered solution
Finite element method

ABSTRACT

In order to model brittle fracture, we have implemented a two and three dimensional phase-field method in the commercial finite element code Abaqus/Standard. The method is based on the rate-independent variational principle of diffuse fracture. The phase-field is a scalar variable between 0 and 1 which connects broken and unbroken regions. If its value reaches one the material is fully broken, thus both its stiffness and stress are reduced to zero. The elastic displacement and the fracture problem are decoupled and solved separately as a staggered solution.

The approach does not need predefined cracks and it can simulate curvilinear fracture paths, branching and even crack coalescence. Several examples are provided to explain the advantages and disadvantages of the method. The provided source codes and the tutorials make it easy for practicing engineers and scientists to model diffuse crack propagation in a familiar computational environment.

1. Introduction

Fracture is one of the main failure modes for engineering materials. However, most of the time design codes apply large safety factors to avoid its manifestation. Additionally, to the devastating consequence of a brittle failure, their evolution is difficult to study in practice. Therefore, predicting the initiation and the propagation path of a fracture is of great importance for practicing engineers and scientists.

The original theory to understand brittle crack evolution was introduced first by Griffith [1], then a new metric, called the stress intensity factor, was proposed by Irwin [2] to account for the microscopic plasticity near the crack tip, even for macroscopically brittle materials [3,4]. They considered crack propagation as a stability problem: if the energy release rate reaches a critical value, the crack is able to open. The original theory describes crack propagation adequately, but it is insufficient to account for initiation, curvilinear crack paths, benching or coalescence.

Nowadays several methods are available to model crack propagation in solids. These methods can be categorized into two major groups depending on how they account for the supposed discontinuity: discrete or diffuse. Using discrete methods, such as node splitting [5], cohesive surfaces [6], hybrid discrete and finite element methods [7], the crack can only propagate between elements, therefore its path is strongly mesh dependent. This problem was overcome by the group of Belytschko [8,9] using a local enrichment in the shape functions of a finite elements (XFEM), as well as by Grüses and Miehe [10] with a configurational-force-driven sharp fracture front.

The second group of fracture modeling assumes that the discontinuity in the material is not sharp, but can be interpreted as a smeared damage. This theory led to the development of the phase-field model [11,12]. This way, the weakness of the original approach of Griffith can be overcome by a variational approach based on energy minimization, as proposed by several authors [13–17]. These approaches introduce a regularized sharp crack taken into account by an auxiliary scalar damage variable. This variable is considered as a phase-field establishing the connection between intact and broken materials.

Over almost a decade this method has gained significant visibility due to its flexible implementation. Besides the work of Msekh et al. [18], mostly in-house softwares were developed to model fracture with phase-fields. Unfortunately, the aforementioned paper neglects to reproduce the results of most of the previous implementations [12], and its source code is not available.

In this paper we give a fully functional implementation as an Abaqus/Standard UEL [19] of the phase-field model [20] to study the quasi-static evolution of brittle fracture in elastic solids. Additionally, as a Supplementary material the source code for the UEL and several examples are provided. Our purpose is to make the diffuse crack propagation scheme widely available not only for numerical scientists,

* Corresponding author.
E-mail address: gmolnar.work@gmail.com (G. Molnár).

http://dx.doi.org/10.1016/j.finel.2017.03.002
Received 4 November 2016; Received in revised form 24 February 2017; Accepted 9 March 2017

but for practical applications and design engineers as well.

Furthermore, the provided source codes can be easily developed to account for dynamical effects [21], large deformations [22], path-following [23] or multi-physics problems [24,25]. One of the major advantage of present implementation, is that no additional updates and softwares are necessary, but only the widely available Abaqus/Standard [19] package and a FORTRAN compiler. It can fit into any existing platform and can be parallelized easily.

The quasi-static simulation of brittle fracture phase-field problem is solved using a staggered algorithm [20]. This approach decouples the elastic and the fracture problem. The strategy has proven to been computationally efficient and extremely robust. However, to reach an accurate solution the step size should be chosen carefully.

Our results compare favorably with the originally developed algorithm [20], as well as with other methods. We provide several examples both with the Abaqus input and FORTRAN files for better understanding and further development. The implementation contains 2D plane strain and 3D cases as well.

The paper is structured as follows. In Section 2 the difference between sharp and diffuse (phase-field) crack is explained. Then the coupling between the elastic solution and the phase-field problem is unfolded. Finally the staggered solution and its finite element implementation are given. Section 3 gives numerous examples and benchmark tests to validate and understand the simulation process. We also highlight the effect of most of the numerical parameters, such as the time step, length scale parameter or even mesh density. Finally in Appendix B a detailed description is given to guide the users in the development of their own models.

2. Methods

2.1. Phase field approximation of diffuse crack topology

To introduce the concept of a diffuse crack topology, let us consider an infinite one directional bar aligned along the x axis with a cross section Γ (see Fig. 1a). Let us assume a fully opened crack at x=0. If function $d(x)$ describes the damage, a sharp crack shown in Fig. 1b is a Dirac delta function. Its value is zero everywhere except at x=0, where

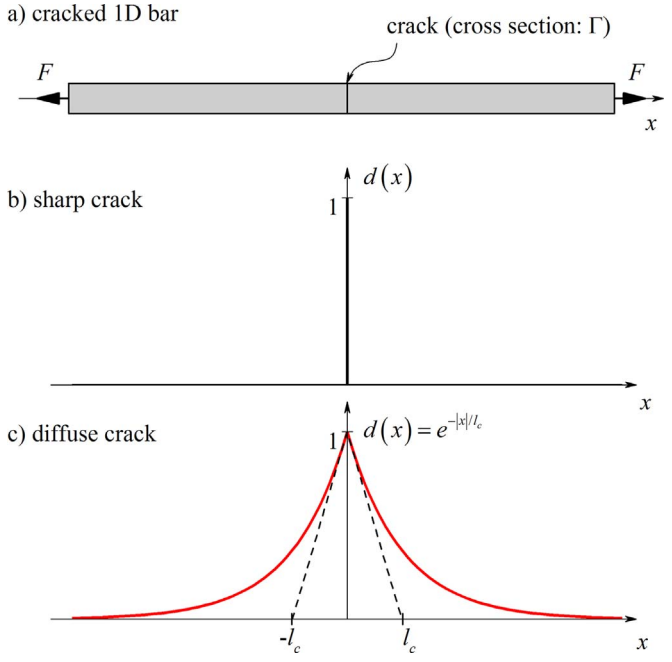

Fig. 1. (a) 1D bar with a crack at the middle with the cross section Γ. (b) Phase-field for sharp crack at x=0. (c) Diffuse crack at x=0 modeled with function (1) and length scale parameter l_c.

$d(0) = 1$. Variable $d(x)$ is the crack phase-field function. If its value is zero, the material in unbroken, if its value reaches 1, it is fully broken.

Following the idea that the crack itself is not a discrete phenomenon, but initiates with micro-cracks and nano-voids, we introduce an exponential function to approximate the non-smooth crack topology:

$$d(x) = e^{-|x|/l_c}, \tag{1}$$

where l_c is the length scale parameter and $d(x)$ represents the regularized or diffuse crack topology. Basically, with this idea the sharp crack is diffused as shown in Fig. 1c. By $l_c \to 0$ the sharp case is recovered. Function (1) has the property $d(0) = 1$ and at the limits $d(\pm\infty) = 0$.

It is the solution for the homogeneous differential equation [12]:

$$d(x) - l_c^2 d''(x) = 0 \quad \text{in} \quad \Omega, \tag{2}$$

subject to the Dirichlet-type boundary condition shown above. The variational principle of strong form (2) can be written as:

$$d = \text{Arg}\left\{ \inf_{d \in W} I(d) \right\}, \tag{3}$$

where

$$I(d) = \frac{1}{2} \int_\Omega (d^2 + l_c^2 d'^2) dV, \tag{4}$$

and $W = \{d | d(0) = 0, d(\pm\infty) = 0\}$. Now observe that the integration over volume $dV = \Gamma dx$ gives $I(d = e^{-|x|/l_c}) = l_c \Gamma$. Thus, the fracture surface is related to the crack length parameter. As a consequence, we may introduce a fracture surface density with the help of the phase-field function by:

$$\Gamma(d) = \frac{1}{l_c} I(d) = \frac{1}{2l_c} \int_\Omega (d^2 + l_c^2 d'^2) dV = \int_\Omega \gamma(d, d') dV, \tag{5}$$

where $\gamma(d, d')$ is the crack surface density function in 1D. Similarly, in multiple dimensions it can be expressed as:

$$\gamma(d, \nabla d) = \frac{1}{2l_c} d^2 + \frac{l_c}{2} |\nabla d|^2. \tag{6}$$

It can be seen that the gradient of the phase-field plays a significant role in the description.

2.2. Strain energy degradation in the fracturing solid

To couple the fracture phase-field with the deformation problem, we can write the potential energy of a solid body as:

$$\Pi^{\text{int}} = E(\mathbf{u}, d) + W(d), \tag{7}$$

where $E(\mathbf{u}, d)$ is the strain and $W(d)$ is the fracture energy. Let $\Omega \subset \mathbb{R}^\delta$, be the reference configuration of a material body with dimension $\delta \in [1 - 3]$, and $\partial\Omega \subset \mathbb{R}^{\delta-1}$ its surface. The crack and the displacement field is studied in the range of time $T \subset \mathbb{R}$. Consequently we can introduce the time dependent crack phase-field:

$$d: \begin{cases} \Omega \times T \to [0, 1] \\ (\mathbf{x}, t) \to d(\mathbf{x}, t). \end{cases} \tag{8}$$

and the displacement field:

$$\mathbf{u}: \begin{cases} \Omega \times T \to \mathbb{R}^\delta \\ (\mathbf{x}, t) \to \mathbf{u}(\mathbf{x}, t). \end{cases} \tag{9}$$

In Eq. (7), the internal potential can be written:

$$E(\mathbf{u}, d) = \int_\Omega \psi(\boldsymbol{\varepsilon}(\mathbf{u}), d) dV, \tag{10}$$

where $\psi(\boldsymbol{\varepsilon}, d)$ is the potential energy density:

$$\psi(\boldsymbol{\varepsilon}, d) = g(d) \cdot \psi_0(\boldsymbol{\varepsilon}). \tag{11}$$

$\psi_0(\boldsymbol{\varepsilon})$ is the elastic strain energy and $g(d)$ is a parabolic degradation

function: $g(d) = (1-d)^2 + k$ and k is a small number responsible for the stability of the solution [12]. In this work we do not consider anisotropic energy degradation [12] (or sometimes refereed to as asymmetric tension and compression energy release), because the examples are primarily tensile stress dominant and no crack closure is modeled. However, there are several methods, which can be used to develop the provided source codes to take the positive (tensile) and negative (compression) energy into account. One of the first study, which decomposed the potential energy into two parts was published by Miehe et al. [12]. After the spectral decomposition of the strain tensor [26], they have assumed that the positive eigenvalues (with the corresponding basis) contribute to the tensile energy as the negative ones to the compression energy. The greatest disadvantage of this approach is that due to the asymmetric degradation (history effect) in the energies, the summation of the positive and negative part creates an unsymmetrical stiffness matrix, which is computationally much more expensive than a symmetric one. Moës et al. [27] proposed a different decomposition, which results in symmetrical constitutive relations. However, the stiffness tensor is still dependent upon the spectral decomposition and thus upon the applied strain. This causes the initially linear problem to become highly non-linear. To overcome this problem, a Newton-type solver with a constant tangent matrix during the same load step can be helpful. In this paper our aim is to give a clear and transparent code which can then be developed either with anisotropic energy degradation [12], dynamic fracture [21] or crack tip enrichment [23], therefore mostly isotropic energy degradation is considered.

Assuming linear elasticity in the unbroken solid, the elastic energy density can be calculated as follows:

$$\psi_0(\boldsymbol{\varepsilon}) = \frac{1}{2}\boldsymbol{\varepsilon}^T \mathbf{C_0} \boldsymbol{\varepsilon}, \tag{12}$$

where $\mathbf{C_0}$ is the materials linear elastic stiffness matrix (in Voigt notation), and $\boldsymbol{\varepsilon}$ if the vector containing the strain components. It is calculated using small strain theory: $\boldsymbol{\varepsilon} = \frac{1}{2}[(\nabla \mathbf{u})^T + \nabla \mathbf{u}]$, where $\mathbf{u}$ is the vector of displacements.

Due to damage, the elastic energy is degraded with function $g(d)$. By calculating its first derivative with respect to the strain tensor (Cauchy stress):

$$\boldsymbol{\sigma} = g(d) \cdot \boldsymbol{\sigma}_0 = [(1-d)^2 + k] \cdot \boldsymbol{\sigma}_0 = [(1-d)^2 + k] \cdot \mathbf{C}_0 \boldsymbol{\varepsilon}. \tag{13}$$

it can be seen, that similarly to the energy, $g(d)$ has a direct effect on it as well. Finally the same can be written for the stiffness:

$$\mathbf{C} = g(d) \cdot \mathbf{C}_0. \tag{14}$$

As a result, it is clear that the damage variable, represented by the phase-field, directly affects the stress and the stiffness of the material. If its value reaches one, no stress or stiffness will be found in the element.

The second term in Eq. (7) stands for the energy due to fracture and can be calculated as:

$$W(d) = \int_\Omega g_c \gamma(d, \nabla d) dV \tag{15}$$

where W is the sum of all the fracture surfaces multiplied by g_c, the critical energy release rate.

After the internal potential energy, the external component can also be formulated as follows:

$$\Pi^{\text{ext}} = P(\mathbf{u}) = \int_\Omega \bar{\boldsymbol{\gamma}} \cdot \mathbf{u} dV + \int_{\partial\Omega} \bar{\mathbf{t}} \cdot \mathbf{u} dA \tag{16}$$

where $\bar{\boldsymbol{\gamma}}$ and $\bar{\mathbf{t}}$ are respectively the prescribed volume and boundary forces.

2.3. Staggered solution for phase-field fracture

For problems, where unstable crack propagation is present the static monolithic solution [12] tends to become numerically unstable as well. When the crack starts to propagate, due to the newly degraded stiffness matrix, the internal stress field rearranges [20,23] and the implicit solver stumbles to find a stable equilibrium solution.

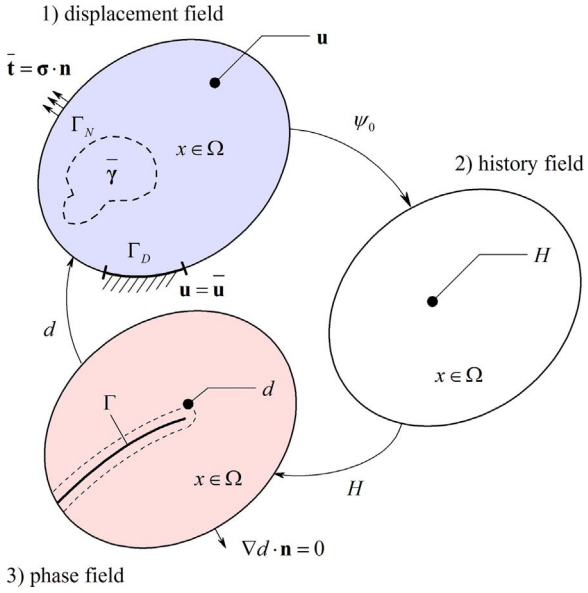

Fig. 2. Illustration of the split scheme phase-field problem in elastic solids.

In order to have a stable implicit formulation the solution is decoupled as follows.

The schematic illustration of the split scheme is shown in Fig. 2. The problem can be split into two quasi independent minimization procedures. First we can write the functional to solve the fracture topology:

$$\Pi^{\text{int}} \simeq \Pi^d = \int_\Omega [g_c \gamma(d, \nabla d) + (1-d)^2 H] dV \tag{17}$$

where we use a so-called history variable:

$$H = \begin{cases} \psi_0(\boldsymbol{\varepsilon}) & \text{if } \psi_0(\boldsymbol{\varepsilon}) > H_n \\ H_n & \text{otherwise,} \end{cases} \tag{18}$$

where H_n is the previously calculated energy history at step n. This field weakly couples the displacement and phase-field. Furthermore it enforces the irreversibility of the damage ($\dot{d} \geq 0$). Thus, the history field satisfies the Karush–Kuhn–Tucker conditions [23]:

$$\psi_0 - H \leq 0, \quad \dot{H} \geq 0, \quad \dot{H}(\psi_0 - H) = 0, \tag{19}$$

both for loading and unloading, therefore no penalty term is necessary in contrast to the monolithic scheme [12].

Then with a fixed d, the displacement field is calculated:

$$E(\mathbf{u}, d) - \Pi^{\text{ext}} \simeq \Pi^u = \int_\Omega [\psi(\mathbf{u}, d) - \bar{\boldsymbol{\gamma}} \cdot \mathbf{u}] dV - \int_{\partial\Omega} \bar{\mathbf{t}} \cdot \mathbf{u} dA \tag{20}$$

By taking the variation of both energies ($\delta\Pi^d = 0$, $\delta\Pi^u = 0$), the corresponding Eulerian equations can be written (strong form) for the displacement:

$$\begin{aligned} &\delta\Pi^u = 0 \quad \forall\, \delta\mathbf{u} \rightarrow \quad \nabla\boldsymbol{\sigma} - \bar{\boldsymbol{\gamma}} = 0 \quad \text{in} \quad \Omega \\ &\boldsymbol{\sigma} \cdot \mathbf{n} = \bar{\mathbf{t}} \qquad\qquad\qquad\quad \text{on} \quad \Gamma_N \\ &\mathbf{u} = \bar{\mathbf{u}} \qquad\qquad\qquad\quad \text{on} \quad \Gamma_D, \end{aligned} \tag{21}$$

and phase-field problems:

$$\begin{aligned} &\delta\Pi^d = 0 \quad \forall\, \delta d \rightarrow \quad \tfrac{g_c}{l_c}(d - l_c^2 \Delta d) = 2(1-d)H \quad \text{in} \quad \Omega \\ &\nabla d \cdot \mathbf{n} = 0 \qquad\qquad\qquad\qquad\qquad\quad \text{in} \quad \Gamma, \end{aligned} \tag{22}$$

where $\boldsymbol{\sigma}$ is the Cauchy stress tensor.

Further information about the mathematical theory on the monolithic [12] and decoupled [20] problems can be found in previous works

of Miehe et al.

2.4. Finite element discretization in Abaqus/UEL

The staggered method is implemented in an Abaqus user defined element (UEL). Using a split scheme operator, the former two minimization problems are solved separately.

Based on the quantities at time t_n (e.g. energy history), a new phase-field is calculated at t_{n+1}:

$$d_{n+1} = \mathrm{Arg}\left\{\inf_d \int_\Omega [g_c \gamma(d, \nabla d) + (1-d)^2 H] dV\right\}, \tag{23}$$

where the history field (H) is calculated according to Eq. (18). With a Newton-Raphson nonlinear solver, the associated linear equation can be solved in close form [20]:

$$\mathbf{K}_n^d \mathbf{d}_{n+1} = -\mathbf{r}_n^d, \tag{24}$$

where $\mathbf{d}_{n+1}$ is the unknown vector containing the new phase-field values of each integration point. $\mathbf{r}_n^d$ is the residue and $\mathbf{K}_n^d$ is the tangent stiffness at time t_n.

To calculate the displacement field at t_{n+1} the phase-field value is used from time t_n:

$$u_{n+1} = \mathrm{Arg}\left\{\inf_u \int_\Omega [\psi(\mathbf{u}, d_n) - \bar{\mathbf{y}}\cdot\mathbf{u}] dV - \int_{\partial\Omega} \bar{\mathbf{t}}\cdot\mathbf{u} dA\right\}. \tag{25}$$

In Eq. (25) $\bar{\mathbf{y}}$, $\bar{t}$ and $\bar{\mathbf{u}}$ are the prescribed Neumann and Dirichlet boundaries at time t_{n+1}. Similarly to the phase-field, this problem can also be solved by a simple linearization:

$$\mathbf{K}_n^u \mathbf{u}_{n+1} = -\mathbf{r}_n^u. \tag{26}$$

All the corresponding residue vectors and stiffness matrices can be found in Appendix A.

To implement the solution in Abaqus two element types are used in a layered manner. Each layer connects at the same nodes, but contributes to the stiffness of different degrees of freedom (DOF). A schematic illustration is depicted in Fig. 3. The first element type has only one DOF (phase-field). The second element type (displacement) contributes to two or three DOF (translational) depending on the dimensionality. In all cases isoparametric elements are used with 4 nodes (2D) and 8 nodes (3D).

In order to visualize the calculated quantities in Abaqus a third layer is added with infinitesimally small stiffness made from a UMAT (user defined material model) [18]. It is used to transfer information

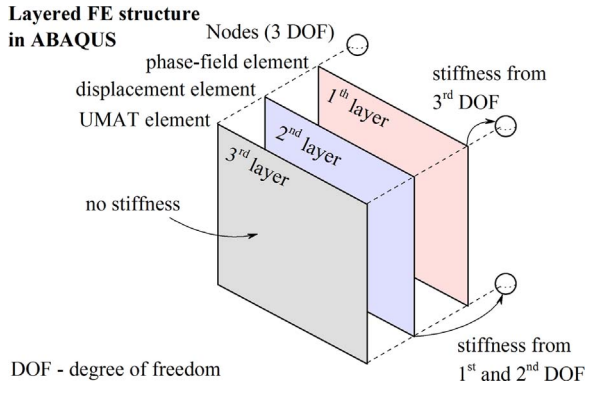

Fig. 3. 2D representation of three layered finite element structure in Abaqus. All nodes have three degrees of freedom (DOF). The first element contributes to the stiffness of the 3rd, the second element to the 1st and 2nd DOF. For post processing purposes a third layer is included made as a UMAT model, which allows to display state dependent variables (SDVs), where the properties are updated from the other two elements. The same approach is applied for the 3D element: the phase-field element has one, and the displacement layer has 3 DOF.

Table 1
Solution dependent variables used to plot the results in two and three dimensions.

Variable	Number of SDV in Abaqus	
	2D (x, y)	3D (x, y, z)
Displacement (stress-strain) element		
Displacement – u_x, u_y, u_z	SDV1-SDV2	SDV1-SDV3
Axial strains – ϵ_x, ϵ_y, ϵ_z	SDV3-SDV4	SDV4-SDV6
Engineering shear strain – γ_{xy}, γ_{xz}, γ_{yz}	SDV5	SDV7-SDV9
Axial stress – σ_x, σ_y, σ_z	SDV6-SDV7	SDV10-SDV12
Shear stress – τ_{xy}, τ_{xz}, τ_{yz}	SDV8	SDV13-SDV15
Elastic axial stress – $\sigma_{x,0}$, $\sigma_{y,0}$, $\sigma_{z,0}$	SDV9-SDV10	SDV16-SDV18
Elastic shear stress – $\tau_{xy,0}$, $\tau_{xz,0}$, $\tau_{yz,0}$	SDV11	SDV19-SDV21
Strain energy – ψ	SDV12	SDV22
Elastic strain energy – ψ_0	SDV13	SDV23
Phase-field – d	SDV14	SDV24
Phase-field element		
Phase-field – d	SDV15	SDV25
History field – H	SDV16	SDV26

from the `common` block and interpolate between integration points. The internal variables are summarized in Table 1 for both 2D plane strain and 3D elements.

The staggered scheme is implemented so that the two elements are connected through only the `common` block, thus with a Newton-Raphson method the following equation system is solved iteratively:

$$\begin{bmatrix} \mathbf{K}_n^d & \mathbf{0} \\ \mathbf{0} & \mathbf{K}_n^u \end{bmatrix} \begin{bmatrix} \mathbf{d}_{n+1} \\ \mathbf{u}_{n+1} \end{bmatrix} = -\begin{bmatrix} \mathbf{r}_n^d \\ \mathbf{r}_n^u \end{bmatrix} \tag{27}$$

In the first iteration at every load step the history and the phase-field is updated for the phase- and displacement field elements. The phase-field problem is solved based on ($H_{n+1} = \psi_{0,n}$), and displacement is based on the phase-field value taken from the end of the previous step (d_n). In Fig. 4 a flowchart shows the basic iteration process.

This solution is slightly different from the staggered scheme proposed by Miehe et al. [20], however it slows down and stabilizes the crack propagation even further. Additional comparison will be given later.

Based on a simple example, Appendix B gives a detailed explanation on how to develop and post-process a model using the newly provided UEL.

3. Benchmark tests and numerical examples

Starting with the simplest case where we compare different methods for one element (analytic, monolithic, staggered), more and more complex cases are introduced. Finally a 3D single notch mode I specimen ends the section. In all cases the relevant numerical parameters are summarized, then the results are shown and interpreted. In all 2D (plane strain) cases the thickness of the element is 1 mm. The mesh is densified where the crack is expected to propagate, the size is specified in the text and the mesh is shown in some of the figures.

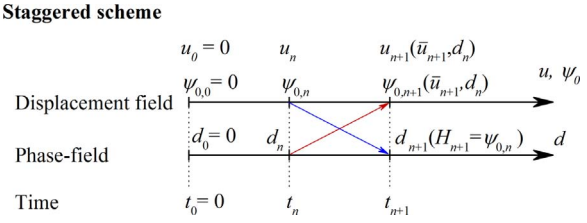

Fig. 4. Flowchart of the staggered solution used to implement the coupled displacement-phase-field solution in Abaqus.

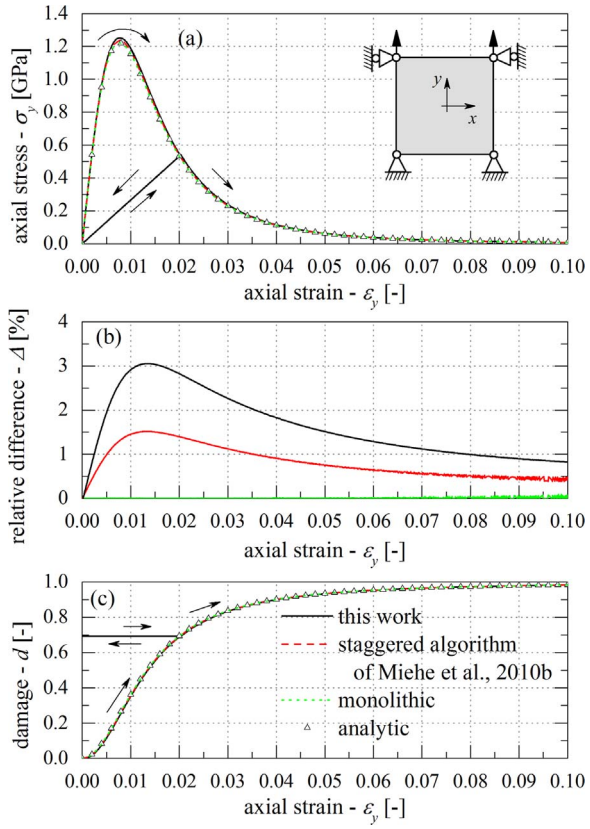

Fig. 5. (a) Axial stress as a function of axial strain for one element subjected to uniaxial tension. (b) Difference between numerically calculated and analytic stress results. (c) Damage phase-field as a function of applied axial strain.

According to the results of Miehe et al. [12] the length scale parameter (l_c) is always taken two times larger than the smallest element around the crack path.

3.1. One element

One 2D plane strain element is the simplest case, where the phase-field model can be understood. In Fig. 5 the boundary conditions and the geometry are shown. The dimensions of the element are 1×1 mm in both x and y direction. The bottom nodes are constrained in both directions, whereas we allow the top nodes to slide vertically.

The Young's modulus of the specimen is set to E=210 kN/mm^2 and the Poisson's ratio to $\nu = 0.3$. The critical energy release rate is $g_c = 5{\cdot}10^{-3}$ kN/mm and the length scale parameter is l_c=0.1 mm. It needs to be noted that we violate our initial criteria concerning the relationship between the mesh size and l_c, thus the theoretical fracture surface in not recovered adequately. Nevertheless, in this section it is not our aim to show actual fracture patterns, only the elementary solution of Eqs. (23) and (25). The deformation is applied in $1000 \times \Delta u_y$ steps, where $\Delta u_y = 10^{-4}$ mm steps.

The input as well as the source file is available for this example in the first Supplementary directory. The practical details are discussed in Appendix B.

The problem introduced in this section can be solved analytically. Due to the discretization the gradient in the crack surface vanishes ($\nabla d = 0$) in Eq. (23). Therefore, if a simple well determined deformation scheme is assumed: $\epsilon_y \neq 0$, $\epsilon_x = \tau_{xy} = 0$, the stresses and the elastic potential energy can be calculated directly: $\sigma_{y,0} = c_{22}\epsilon_y$, where c_{22} is the (2,2) element of the plane strain stiffness matrix: $c_{22} = \frac{E(1-\nu)}{(1+\nu)(1-2\nu)}$. And finally the elastic energy can be calculated as: $\psi_0 = \varepsilon_y^2 c_{22}/2$.

Solving the minimization problem shown in Eq. (23) for one element, and assuming a direct coupling between displacement and phase-fields ($H = \psi_0$) we can show that the damage parameter results in:

$$d = \frac{2H}{\frac{g_c}{l_c} + 2H} = \frac{2\psi_0}{\frac{g_c}{l_c} + 2\psi_0} = \frac{\varepsilon^2 c_{22}}{\frac{g_c}{l_c} + \varepsilon^2 c_{22}}. \tag{28}$$

As well as the y directional axial stress: $\sigma_y = \sigma_{y,0}(1-d)^2$.

Fig. 5a shows the axial stress computed by analytical, monolithic (concerning implementation details can be found in Ref. [23]), and two staggered schemes.[1] A very good agreement can be found between methods. Also the black line shows that after a certain damage not just stresses (as shown in Eq. (13)), but also the stiffness is degraded: $\boldsymbol{C} = (1-d)^2 \cdot \boldsymbol{C}_0$.

Quantitative comparison between the analytically calculated stresses and the numerical results are shown in Fig. 5b. It can be seen that the monolithic solution almost perfectly recovers the analytic solution, whereas the staggered schemes accumulate a small sum of error. This solution compared to Miehe's work [20] shows two times larger error, because the variables are updated only at each time step. In the work of Miehe et al. [20] the displacement field is calculated based on the already determined phase-field. Unfortunately, in Abaqus the two degrees of freedom cannot be isolated and solved separately. Despite the observed difference the error is vary small and by reducing the time step, it can be eliminated. Therefore, we conclude that both staggered schemes carry the same disadvantage. The error caused by the deviation can be neglected with respect to the incredible robustness gained by the methods [23,20].

Stability problems appear in the monolithic solution, when the crack starts to propagate and due to the quick stiffness and stress reduction in a small amount of elements, the initial prediction soon differs markedly from the solution. Due to the abrupt change in the stiffness the stress needs to redistribute, and the Newton-Raphson method needs a significant amount of internal iterations to converge. Of course due to the fact that in a one element model, no stress redistribution appears, we do not have any stability problem.

Finally, Fig. 5c shows the governing phase-field as a function of the applied axial strain. It can be observed that the staggered algorithm satisfies the irreversibility criterion ($\dot{d} \geq 0$) without any Penalty parameter as used in the monolithic scheme [12].

3.2. Single edge notched test

Our second benchmark test is the well known single edge notched tensile and shear sample. The geometry and the boundary conditions are depicted in Fig. 6a. The bottom side of the rectangular specimen is fixed, while the top side is moved. The stiffness is set to: E=210 kN/mm^2 and $\nu = 0.3$. Fracture properties are taken identical to Ref. [20] for direct comparison: $l_c = 0.0075$ mm, $g_c = 2.7{\cdot}10^{-3}$ kN/mm.

The finite element mesh of ≈22, 000 elements is used. The region around the crack path is refined in order to reach the maximum of h=0.001 mm mesh size.

Tensile loading is applied by $\Delta u = 10^{-4}$ mm for 500 steps, then $\Delta u = 10^{-5}$ mm to precisely follow the overall propagation. While the shear deformation was applied in $\Delta u = 10^{-4}$ mm for 1000 steps. Then the step size was reduced similarly to the tensile case to $\Delta u = 10^{-5}$ mm. The change in the step size is applied to be consistent with the results of Miehe et al. [12,20].

The fracture pattern for the two limit cases are shown in Fig. 6b and c. While for the tensile case ($\alpha = 90°$), the crack is horizontal, for the pure shear case we see a curved crack path initiating with a $\beta = 61°$ angle from the direction of the deformation. The crack pattern is in agreement with both works of Miehe et al. [12,20]. As well as by

[1] Due to lack of available space the concerning line colors are shown in Fig. 5c.

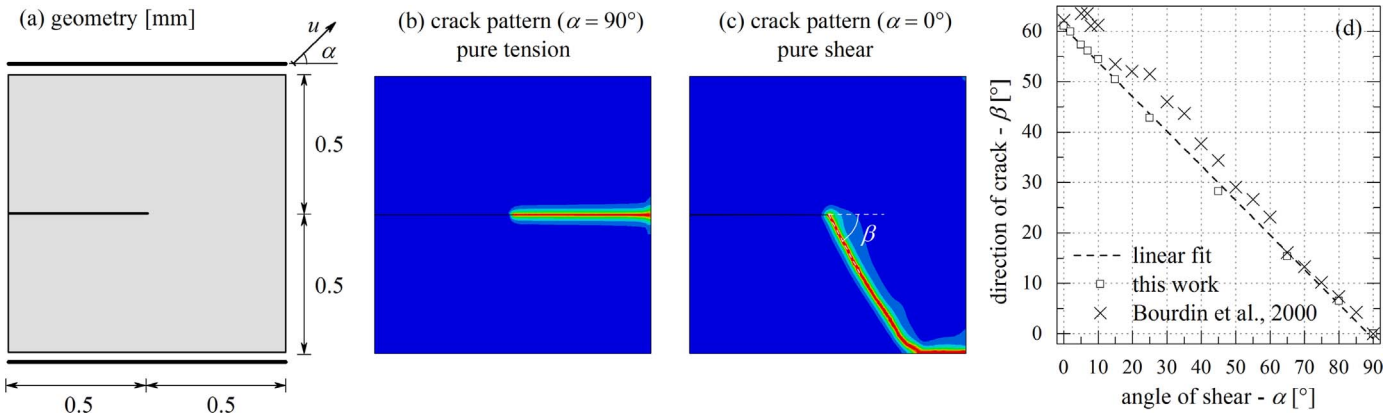

Fig. 6. (a) Geometry and boundary conditions of single edge notched specimen. (b) Fracture pattern for unidirectional tension ($\alpha = 90°$). (c) Fracture pattern for pure shear deformation ($\alpha = 0°$). (d) Crack angle (β) as a function of loading direction (α) with linear fit and the work of Bourdin et al. [16] (variational model).

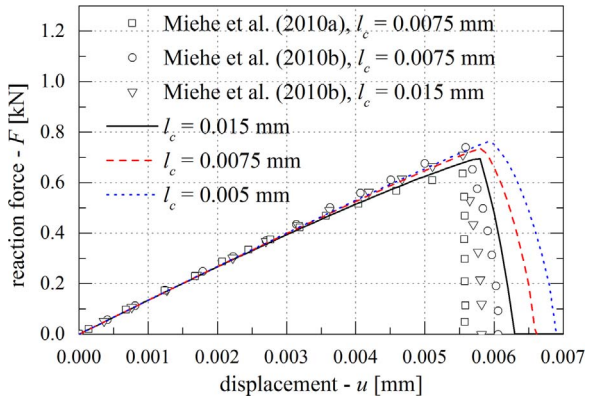

Fig. 7. Reaction force for the uniaxial tensile test using different length scale parameters (l_c) along with results by Miehe et al. [12,20] (symbols).

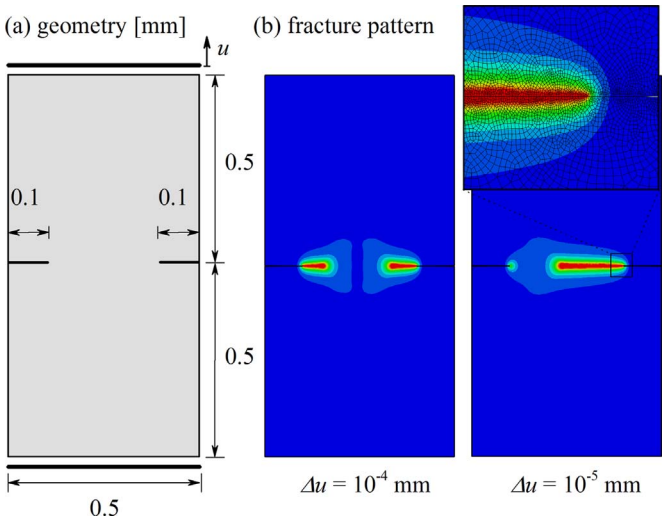

Fig. 8. (a) Geometry and boundary conditions for the double notched specimen. (b) Fracture pattern with $\Delta u = 10^{-4}$ mm. (c) Fracture pattern with $\Delta u = 10^{-5}$ mm.

gradually changing α a linear transition is observed in β. There is excellent agreement with the work of Bourdin et al. [16] as shown in Fig. 6d.

In Fig. 7a the y directional reaction force is shown for the tensile specimens for different length scale parameters (l_c) along with previous results by Miehe et al. [12,20] are shown next to our results. It can be seen that the maximum reaction force value is in agreement, only a small deviation in the propagation period can be observed. Similarly, as it is shown between the monolithic [12] and staggered scheme [20], the crack propagation calculated by our solution is slowed down ever further. This result causes no problem, because these implicit methods carry no dynamic meaning (due to lack of mass [21]). Additionally, as will be discussed later, by reducing the time step the solution converges to the monolithic one.

Due to the large size of the input files only a smaller tensile test with ≈4000 elements (h=0.005 mm) is included as Supplementary material in the second folder.

3.3. Symmetric double notched tensile test

Using a double notched specimen shown in Fig. 8a we have studied the effect of load step and finite element size. The following material properties are used: E=210 kN/mm^2, $\nu = 0.3$, $l_c = 0.0075$ mm, $g_c = 2.7 \cdot 10^{-3}$ kN/mm.

The sample is meshed randomly with a refined zone at the middle (for details see Fig. 9a and b). The crack edges and the dotted line are meshed with h, while the dashed lines with 10 h size finite elements. The transition between the different zones are linear. The deformation is applied with a constant rate using $\Delta u = 10^{-6}$ mm steps.

In Fig. 9c the reaction force is shown as a function of the displacement. While Fig. 9 part d shows the maximum force as a function h. It can be seen that there are cases (shown with crosses) which do not fracture until u=0.01 mm, therefore the maximum reaction force cannot be defined. However, if the mesh is densified a gradual convergence appears. Red dashed line shows the value of $l_c/2$, which was suggested as a minimum elements size by Miehe et al. [12]. According to their analysis, this is the value, where the spatial integration of the damage variable recovers sufficiently the analytic fracture surface. The choice of the length scale parameter was arbitrary in this case. However, in real materials the crack propagation phenomenon can be understood as multi-scale damage. In most of the materials (e.g. bone [28], glasses [29] or even metals [30]) the crack front is not precisely identifiable. Therefor, it could be possible to define a damage length scale parameter as a real material property. However, this topic exceeds the aim of present paper.

The time step has also a significant effect on not only the stress field, but the governing crack pattern as well. Fig. 8b shows the effect of the random, consequently unsymmetrical mesh. If the time step is not small enough, the crack appears symmetrically. However, after reducing the load increment – due to the random mesh – more potential energy gathers at one side, initiating the crack faster at that notch.

The deviation due to too large load steps is visible in the reaction

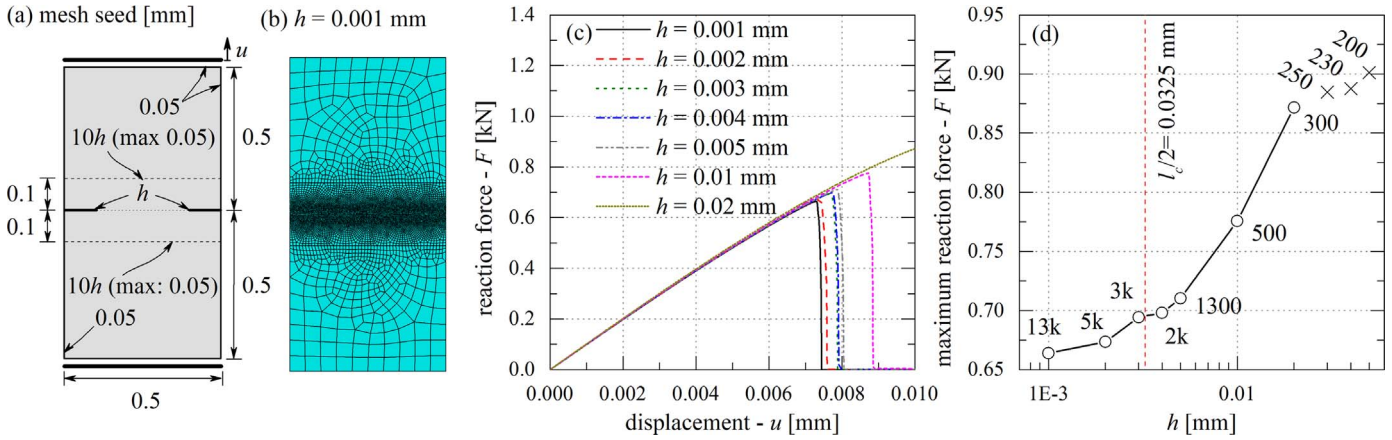

Fig. 9. (a) Schematic illustration of mesh seed distribution. (b) Finite element mesh for h=0.001 mm. (c) Reaction force as a function of displacement. (d) Maximum reaction force as a function of mesh size (h) (next to each data point the approximate amount of finite elements are plotted; "k" stands for thousand). (For interpretation of the references to color in this figure legend, the reader is referred to the web version of this article).

force diagram. Thanks to the robustness of the solution, the Newton-Raphson solver always finds a local equilibrium, however the precision of the solution remains questionable. In Fig. 10a and b it can be seen that the maximum reaction force depends strongly on Δu. By reducing Δu, the maximum reaction force reduces as well. When the load step is small enough ($\Delta u = 10^{-5}$ mm) a convergence is observed.

Another interesting test can be conducted by deforming the sample until u=0.008 mm (under 0.8 s pseudo time), and then stopping the displacement but continuing the calculation. Fig. 10c shows the reaction force for a sample which was deformed using $\Delta u = 10^{-5}$ mm displacement steps ($\Delta t = 10^{-3}$ s time steps) until u=0.008 mm, then the top displacement was frozen but the iteration was continued. An interesting creep like phenomenon can be observed. Even with the static scheme if the crack propagation is unstable, the method can find the fully opened crack state. Furthermore, it is interesting to see, that if the time step is varied the pseudo dynamics of the crack is different. In Fig. 10c we plotted the reaction force for different time steps. If Δt was left 10^{-3} s the crack finished propagating the same time, as when the top side was moved ($t \approx 0.84$ s). But if the step size was reduced, the crack accelerated.

One of the disadvantages of the decoupled solution, is that the amount of "staggering" affects the time dependent response significantly. Therefore, it is highly recommended to conduct a sensitivity study when developing a new model. The symmetric double notch model is included as a Supplementary file in the third directory.

3.4. Asymmetric double notched tensile specimen

After the simple cases we are going to present a few complex ones to show the utility of the new implementation. To study the coalescence of the cracks a well studied [31,32] asymmetric double notch specimen is used. The exact geometry is depicted in Fig. 11a. The following material properties are used: E=210 kN/mm^2, $\nu = 0.3$, $l_c = 0.2$ mm, $g_c = 2.7 \cdot 10^{-3}$ kN/mm. The mesh is well refined and contains ≈38, 000 elements, with the size of h=0.1 mm around the crack path. The tensile deformation is applied by $\Delta u = 10^{-4}$ mm for 400 steps, then $\Delta u = 10^{-5}$ mm for the rest of the simulation to follow precisely the governing fracture pattern.

The appearing fracture pattern is shown in Fig. 11b.

The eventually obtained fracture pattern is in excellent agreement with previous results [27,31,32].

3.5. Notched bi-material tensile test

This case study is a tensile specimen made of two materials. The upper material is stiffer and its fracture toughness if higher (E=377 kN/mm^2, $\nu = 0.3$, $l_c = 0.3$ mm, g_c=0.01 kN/mm), whereas the lower material is 10 times softer (E=37.7 kN/mm^2, $\nu = 0.3$, $l_c = 0.3$ mm, g_c=0.001 kN/mm) and has an initial notch. The specimen is tensioned parallel to the separating line. The geometry and boundary conditions are shown in Fig. 12a.

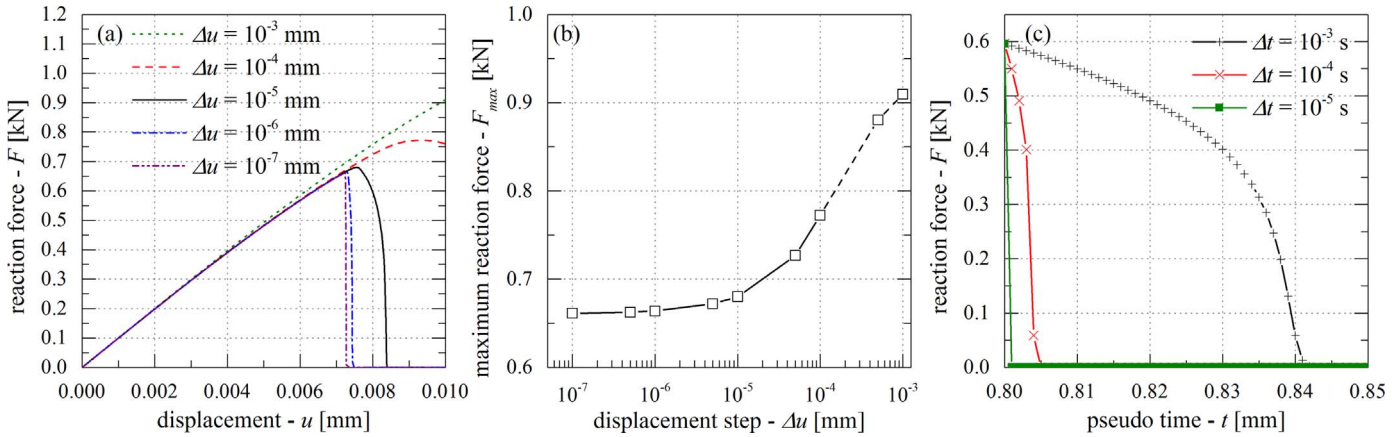

Fig. 10. Reaction force as a function of displacement: (a) different Δu; (b) maximum force as a function of Δu; (c) deformation stopped at u=0.008 mm with $\Delta u = 10^{-5}$ mm and the calculation is continued with different time steps.

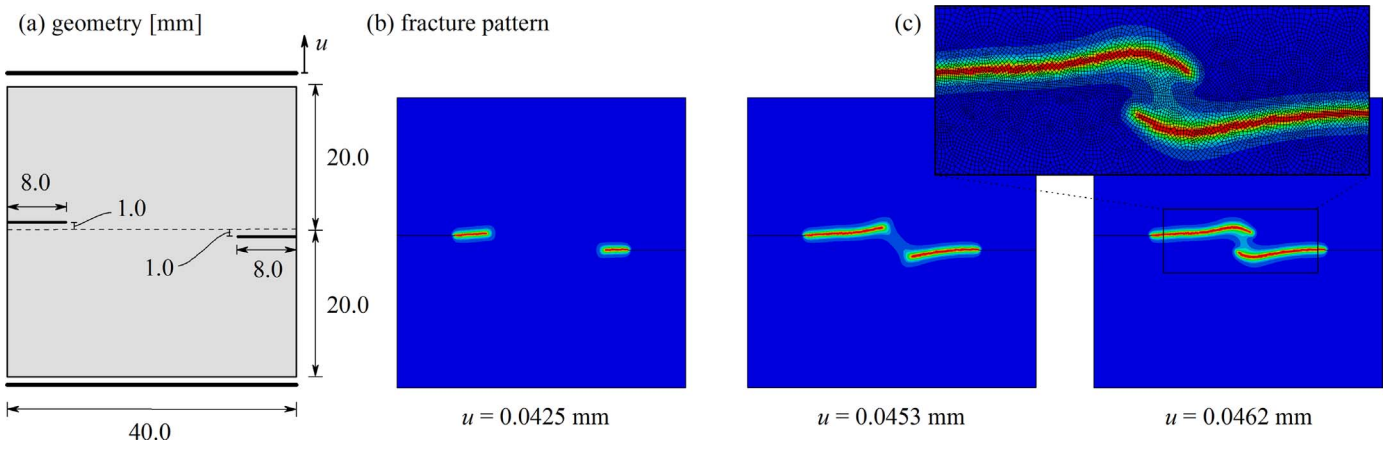

Fig. 11. (a) Geometry and boundary conditions for the double notched asymmetric tensile test. (b) Fracture pattern at different displacement steps.

The model consists of ≈15, 000 elements, with a refinement of h=0.1 mm. The deformation is applied by $\Delta u = 10^{-4}$ mm for 400 steps, then $\Delta u = 10^{-5}$ mm for the rest of the simulation.

The aim of this benchmark test is to show that our implementation is capable of modeling the crack branching phenomenon.

The reaction force is shown in Fig. 12b. It can be recognized that mostly the loading is carried by the hard material, therefore when the fracture occurs in the soft part, it does not affect the overall response significantly.

Fig. 13 shows the evolution of the damage in the specimen. After initiation the fracture propagates normally until reaching the material transition zone. Then, since branching requires less energy than continuing into the hard material after a short period the damaged zone becomes larger, and the crack separates along the interface. Fig. 13e shows that after a large deformation even the stronger material starts to break, and the reaction force to reduce. The aim of this benchmark test is to show crack branching, therefore the finite element mesh is densified at the center. The crack in the stiffer material is thus wider because the finite element size at that area is larger.

3.6. Symmetric three point bending test

Consider a symmetric three point bending test depicted in Fig. 14a. The material parameters are the following: E=20.8 kN/mm^2, $\nu = 0.3$, l_c=0.03 and 0.06 mm, g_c=0.0005 kN/mm. The finite element mesh consists of ≈28, 000 elements with a refinement of h=0.002 mm at the middle. The loading is applied with $\Delta u = 10^{-4}$ mm for 360 steps, then $\Delta u = 10^{-5}$ mm for the rest of the simulation.

As shown in Fig. 14a, the left and right sides of the beam are considered elastic according to the suggestions of Moës [27]. Due to the singularity caused by the constrained nodes, if the material remained non-linear, the initial notch would have significantly less effect and the crack would initiate from one of the corners.

In Fig. 14b the reaction force is shown for isotropic and anisotropic energy degradation. For the latter, Eq. (18) is modified in order to degrade only the tensile part of the energy:

$$H = \begin{cases} \psi_0^+(\boldsymbol{\varepsilon}) & \text{if } \psi_0^+(\boldsymbol{\varepsilon}) > H_n \\ H_n & \text{otherwise} \end{cases}, \tag{29}$$

where ψ_0^+ is the tensile part of the overall potential energy: $\psi = g(d)\psi_0^+ + \psi_0^-$. It can be calculated as follows:

$$\psi_0^{\pm} = \frac{E\nu}{(1+\nu)(1-2\nu)}\langle tr(\boldsymbol{\varepsilon})\rangle_{\pm}^2 + \frac{E}{2(1+\nu)}(\langle\varepsilon_2\rangle_{\pm}^2 + \langle\varepsilon_2\rangle_{\pm}^2). \tag{30}$$

Functions $\langle\rangle_{\pm}$ stand for: positive $\langle x\rangle_+ = (x + |x|)/2$ and negative $\langle x\rangle_- = (x - |x|)/2$ part, while $\varepsilon_{1,2}$ are the principal strains. Details concerning the stress calculation and the tangent stiffness can be found in Ref. [27].

Fig. 7b shows only a slight difference in the macroscopic response if

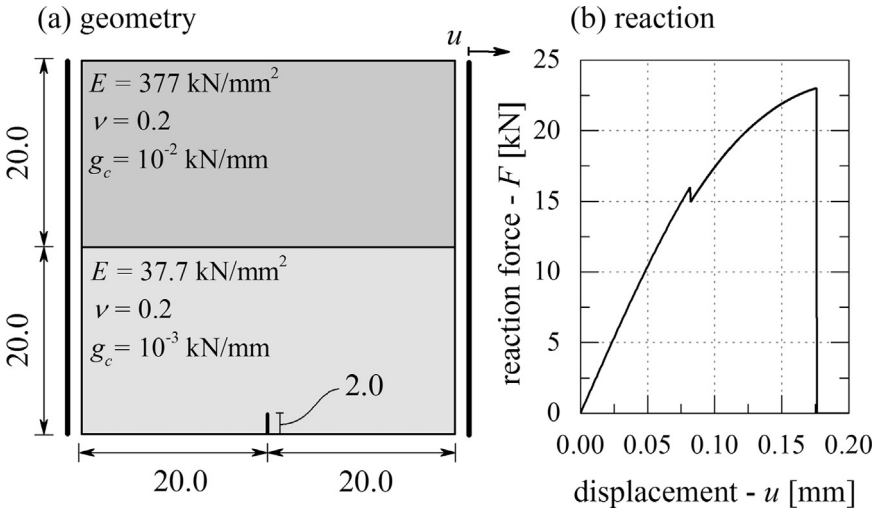

Fig. 12. Geometry, material properties and boundary conditions for the bimaterial tensile test. The specimen is made of two materials with significantly different stiffness and fracture properties.

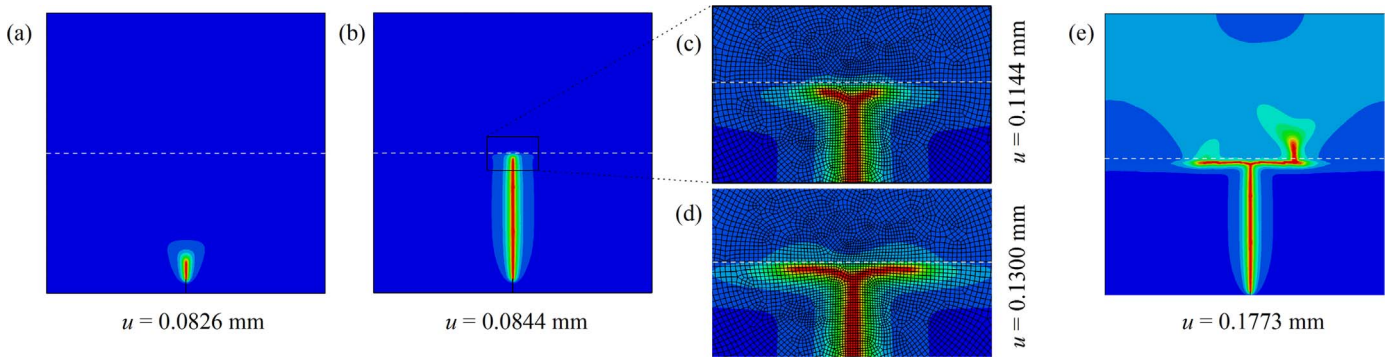

Fig. 13. Fracture pattern for different load steps. In parts (c) and (d) a close lookup is given at the branching area.

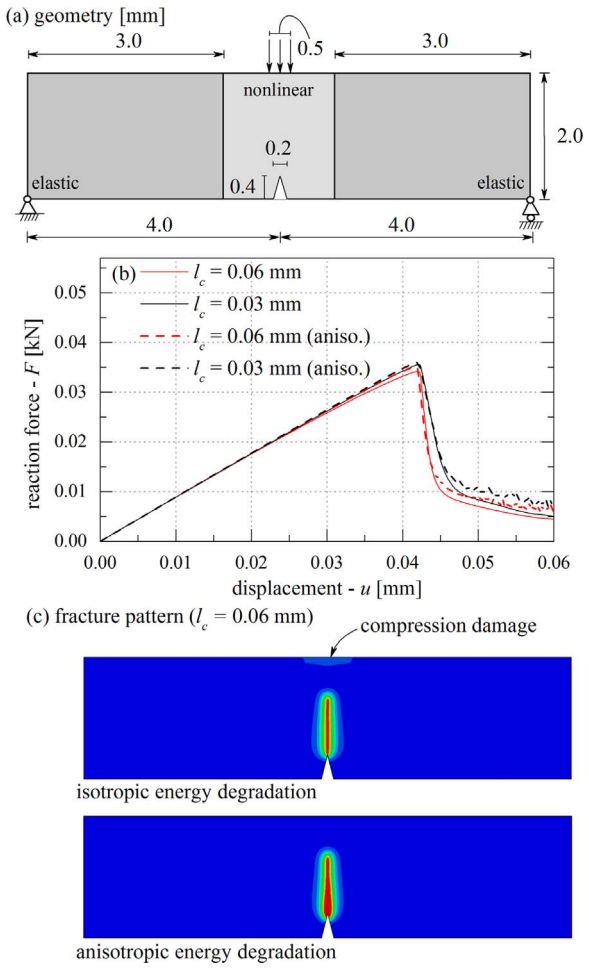

Fig. 14. (a) Geometry and boundary conditions for the symmetric three point bending test. (b) Reaction force as a function of applied displacement for two different l_c values. The symmetric degradation case is shown with solid line and the asymmetric one with dashed line. (c) Fracture pattern for l_c=0.06 mm with symmetric and asymmetric energy degradation. The damaged area caused by compressive damage is highlighted in the upper figure.

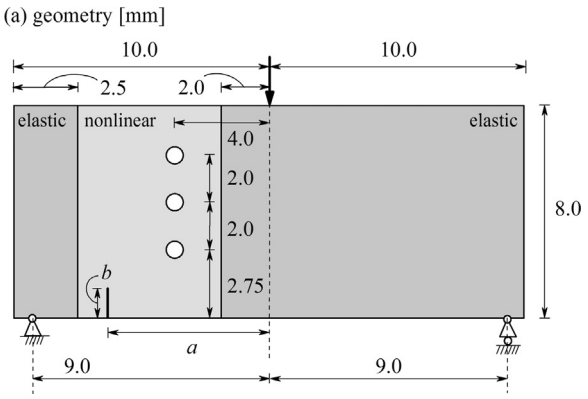

Fig. 15. Geometry and boundary conditions for the perforated asymmetric bending test. The holes are 0.5 mm in diameter. Example 1: a=6 mm, b=1 mm. Example 2: a=5 mm, b=1.5 mm.

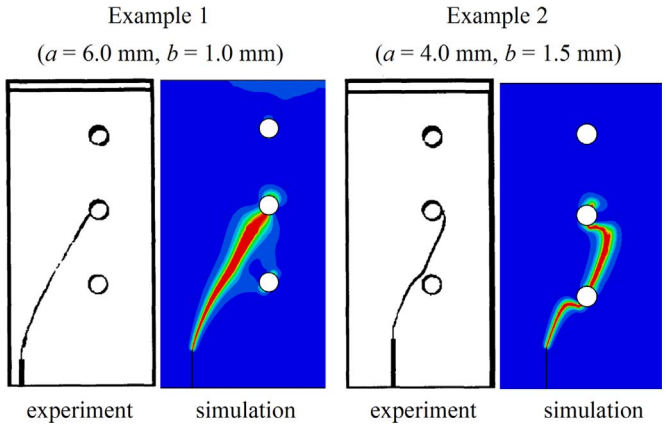

Fig. 16. Fracture pattern for the two cases compared with experimental results of Bittencourt's et al. [33].

only the tensile energy is degraded. Compared to the effect of the length scale parameter, it is negligible. However, in Fig. 14c the fracture pattern shows that if compression can cause damage a small fracture zone appears under the applied load. This becomes more and more significant if the loading is employed using a concentrated force. Due to the singularity this can cause the crack to propagate not from the notch but from the loading area.

3.7. Perforated asymmetric bending test

With the asymmetric three point bending test a curvilinear crack trajectory can be studied. The evolution of the crack path strongly depends on the precise position of the holes [33]. In Fig. 15 the geometry and the boundary conditions are shown. Similarly to the symmetric problem, here the sides are considered elastic. The non-linear material parameters are the following: E=20.8 kN/mm^2, ν = 0.3, l_c=0.025 mm, g_c=0.001 kN/mm. The mesh is refined around the holes and the notch (h=0.01 mm). The model contains ≈60,000 elements.

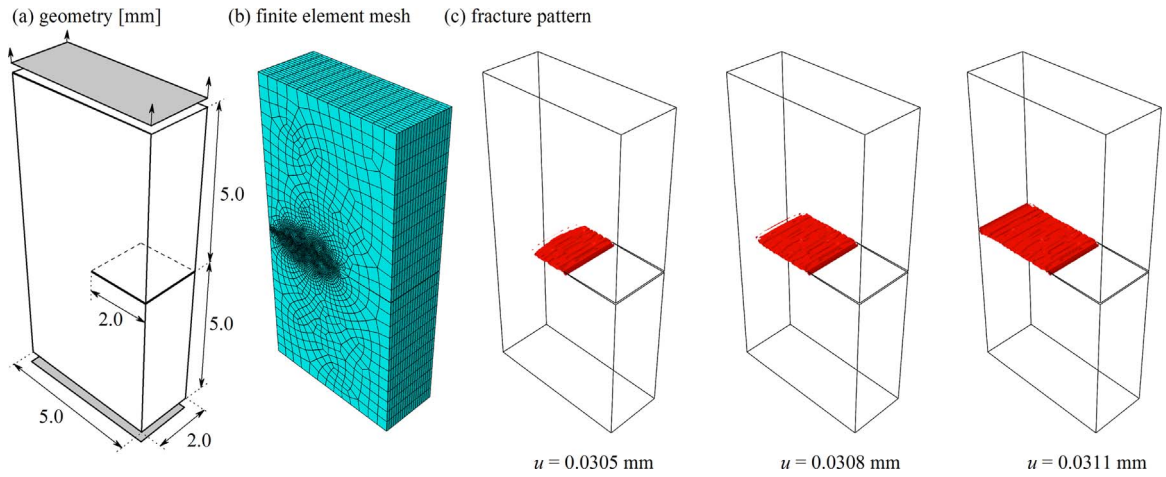

Fig. 17. (a) Geometry and boundary conditions for the three dimensional single edge notched tensile test. (b) Finite element mesh. (c) Fracture pattern: isosurface of the phase-field with the value above 0.97.

The bending load is applied with: $\Delta u_y = 10^{-3}$ mm for 150 steps, then $\Delta u = 10^{-4}$ mm for the rest of the simulation.

Two examples are studied, similarly to Ref. [33]. The geometrical differences can be found in Fig. 15.

It is a great example, because by modifying the initial size and position of the notch, the governing fracture pattern can be altered. If the crack is placed closer to the holes and its initial length is larger, the governing fracture approaches the second hole from the right. However, if it is further away, the fracture appears from the left.

Fig. 16 shows that the crack pattern is recovered precisely with the phase-field method for the first example. However, the crack collides with the first hole in the second, then follows the experimental results as well. In the phase-field scheme the crack has a finite width. Therefore, if the damaged zone reaches a hole, it attracts the crack, and the fracture cannot pass by. Usually, the second example is not shown in papers dealing with diffuse crack propagation [12,20,34] due to the above mentioned problem. However, we strongly believe that if this method is going to be used by practicing engineers, not only the functional cases should be shown, but the attention needs be drawn to examples where the approach gives less precise results.

3.8. Three dimensional single notched plate

We end this section with a three dimensional case. Similarly to the 2D case, a single edge notched specimen is studied with a mode I crack. The material properties and the geometry are taken according to Ref. [12]: E=20.8 kN/mm^2, $\nu = 0.3$, l_c=0.2 mm, $g_c = 5{\cdot}10^{-4}$ kN/mm with the mesh of ≈54,000 elements, and the refinement of $h = 0.03$ mm. The loading is applied with $\Delta u = 10^{-4}$ mm for 250 steps, then it is reduced to $\Delta u = 10^{-5}$ mm.

Fig. 17a and b show the geometry and the 3D finite element mesh.

To show the crack, the isosurface of the damage phase-field is depicted with the value larger then 0.97 in Fig. 17c. The result is in agreement with the monolithic solution of Miehe et al. [12].

A 3D example containing one element is included as Supplementary material with the corresponding source code.

4. Conclusion

A staggered phase-field model was implemented in the commercial finite element code Abaqus/Standard to simulate brittle fracture in 2D and 3D solids. The implementation was carried out in the framework of a user defined finite element (UEL). To visualize the results, an additional layer of UMAT was included. The solution is given as two (plus one for visualization) finite element layers. Each layer contributes to different degrees of freedom. Depending on the dimensionality each node has two (or three) translational and one phase-field (damage) DOF. The phase-field is a scalar variable which connects broken and unbroken materials. If its value reaches one, both stiffness and stress reduce to zero.

The method is based on the rate-independent variational principle of diffuse fracture. The elastic displacement and the fracture problem are decoupled and solved separately. The connection is established using a so-called history variable, which contains the materials elastic potential energy.

The sources code for both 2D and 3D element are available as Supplementary material with four benchmark examples. Abaqus is one of the most widely used software in practice. Therefore, this implementation enables practicing engineers and scientists to simulate easily not only crack propagation, but initiation, curvilinear paths, branching and even coalescence.

The utility of the method is shown through several examples: starting from one element up to 3D crack propagation.

It was shown that the right choice of the load step is the most important to achieve precise results. The size of the finite elements has small effect on the macroscopic force response if it is smaller than the half of the length scale parameter (l_c).

There remains an important question: is l_c, which controls the diffusion of the crack, a material parameter, or just a numerical one. This can be tested using atomic scale simulations [35,3] as well as microscopic experiments [36].

Present implementation gives a transparent code which can be developed further in order to model large strains [22], plasticity near cracks [37], snap-back effects [23] or even dynamic fracture [21] in glass [38].

Appendix A. Implementation details

To calculate the phase-field fracture problem a split scheme operator is used. The following linear equation system is solved iteratively using a

Newton-Raphson algorithm, updating the tangent matrix and the residue vector at each internal iteration:

$$\begin{bmatrix} \mathbf{K}_n^d & \mathbf{0} \\ \mathbf{0} & \mathbf{K}_n^u \end{bmatrix} \begin{bmatrix} \mathbf{d}_{n+1} \\ \mathbf{u}_{n+1} \end{bmatrix} = - \begin{bmatrix} \mathbf{r}_n^d \\ \mathbf{r}_n^u \end{bmatrix} \tag{A.1}$$

The corresponding residue vector for the phase-field degrees of freedom reads as:

$$\mathbf{r}^d = \int_\Omega \left\{ \left[\frac{g_c}{l_c} d - 2(1-d)H \right] (\mathbf{N}^d)^T + g_c l_c (\mathbf{B}^d)^T \nabla d \right\} dV \tag{A.2}$$

where $\mathbf{N}^d$ is the vector of the shape functions: $\mathbf{N}^d = [N_1 \quad \dots \quad N_b]$ (where b=4 for 2D and b=8 for 3D) and $\mathbf{B}^d$ is a matrix with the spatial derivatives (gradient)[2]:

$$\mathbf{B}^d = \begin{bmatrix} \frac{\partial N_1}{\partial x} & \dots & \frac{\partial N_b}{\partial x} \\ \frac{\partial N_1}{\partial y} & \dots & \frac{\partial N_b}{\partial y} \\ \frac{\partial N_1}{\partial z} & \dots & \frac{\partial N_b}{\partial z} \end{bmatrix}.$$

The phase-field values are calculated on each integration point as: $d = \mathbf{N}^d \mathbf{d}$, where $\mathbf{d}$ is a vector contacting phase-field values on each element node. The local gradient reads similarly as: $\nabla d = \mathbf{B}^d \mathbf{d}$.

In Eq. (A.1) the tangent matrix is calculated as follows:

$$\mathbf{K}^d = \int_\Omega \left\{ \left[\frac{g_c}{l_c} + 2H \right] (\mathbf{N}^d)^T \mathbf{N}^d + g_c l_c (\mathbf{B}^d)^T \mathbf{B}^d \right\} dV. \tag{A.3}$$

The displacement residue can be divided into internal and external parts: $\mathbf{r}^u = \mathbf{f}^{\text{int}} - \mathbf{f}^{\text{ext}}$. The external force vector reads as:

$$\mathbf{f}^{\text{ext}} = \int_\Omega (\mathbf{N}^u)^T \cdot \bar{\boldsymbol{\gamma}} dV + \int_{\partial\Omega} (\mathbf{N}^u)^T \cdot \bar{\mathbf{t}} dA. \tag{A.4}$$

Whereas, the internal one is:

$$\mathbf{f}^{\text{int}} = \int_\Omega \{ [(1-d)^2 + k] (\mathbf{B}^u)^T \boldsymbol{\sigma}_0 \} dV. \tag{A.5}$$

Finally we give the tangent matrix for the displacement field solution:

$$\mathbf{K}^u = \int_\Omega \{ [(1-d)^2 + k] (\mathbf{B}^u)^T \mathbf{C}_0 \mathbf{B}^u \} dV \tag{A.6}$$

Similarly to the phase-field problem $\mathbf{N}^u$ and $\mathbf{B}^u$ are the vector of shape functions and its derivatives used in classic finite elements [39].

Appendix B. Tutorial: one element

Present section shows a simple example, which can be used to create any model in Abaqus/Standard with the staggered fracture model. The problem which is going to be solved is a simple element subjected to a uniaxial tension. This example is shown in the first Supplementary folder (Abaqus input file and FORTRAN code). For results and comparison with other methods see Section 3.

Every problem consists of two files: an Abaqus input file (`*.inp`) and a FORTRAN file (`*.for` or `*.f`, depending on the operation system).

Due to the problem of the allocation of the `common` block for every finite element mesh a new FORTRAN file should be created. The only variable which should be modified in the provided example file is `N_ELEM` (the number of the elements in one layer). Thus, in this case `N_ELEM=1`.

The Abaqus input file is generally written by the software itself, however we can access it before initiating the simulation.

In the first section the parts are created. The nodes are given (`*Node`) and the elements are generated. After creating all the nodes, a command is given to define the phase-field element type (`*User element, nodes=4, type=U1, properties=3, coordinates=2, VARIABLES=8`). This command creates an element with four nodes, in 2D, with three material properties and eight status variables. The status variables are used to transport information from one step to the next. It contains the phase-field value and the history variable at each integration point. For details visit Table 1, where first the displacement then the phase-field variables are listed.

In the next line we define the concerning degree of freedom, in this case only the third. To create the elements after the command: `*Element, type=U1`, the elements are given starting with the serial number then the nodes of the corners in a counterclockwise list: `1, 1, 2, 4, 3`. To assign material properties to the elements a set is created. After which the command `*Uel property, elset=AllPhase` and the properties are given in the next line (where `AllPhase` is the name of the set containing the phase-field elements). The properties are gives as follows: length scale parameter (l_c), fracture surface energy (g_c), thickness.

Similarly the second layer can be created (see example file). When generating the elements, the same node sequence is listed and `N_ELEM` is added to the first digit (serial number): **2**`, 1, 2, 4, 3`. The material properties should be given in the following order: Young's modulus (E), Poisson's ratio (ν), thickness, stability parameter (k, usually a small number).

The third layer is created following the sequence mentioned above. The nodes are listed the third time in the same order while the serial number of the elements shifted again with `N_ELEM`: **3**`, 1, 2, 4, 3`.

Than in the assembly section the nodes are declared, where the boundary conditions are applied. Here an additional set should be defined in order to save only the results from the UMAT elements: `*Elset, elset=umatelem`.

From this point, the loads, boundaries and the analysis is defined usually as it is done in a normal input file.

[2] In 2D it is constructed only from x, y directional components.

A general advise is to create the finite element model using the graphical interface of Abaqus, then replicate the three different layers multiplying the serial number of the elements as it is shown above. Furthermore, adding a line in the `ASSEMBLY` section pointing to the UMAT elements for post-processing purposes. Then creating a job based on the new input file linked to the FORTRAN script.

To visualize the results simply open the concerning `*.odb` file and select the desired solution dependent variable (SDV) in contour plot mode according to Table 1. To remove the white X from the bottom left corner go to: Options/Display Group/Create...and select `ELEM-1.UMATELEM` from the Elements item and press replace. This seems unnecessary in this case, but for many elements the white nodes can dilute the image.

Appendix C. Supplementary data

Supplementary data associated with this article can be found in the online version at http://dx.doi.org/10.1016/j.finel.2017.03.002.

References

[1] A.A. Griffith, The phenomena of rupture and flow in solids, Philos. Trans. R. Soc. Lond. A Math. Phys. Eng. Sci. 221 (582–593) (1921) 163–198.
[2] G.R. Irwin, Fracture, Springer Berlin Heidelberg, Berlin, Heidelberg, 1958, pp. 551–590.
[3] G. Molnár, P. Ganster, A. Tanguy, E. Barthel, G. Kermouche, Densification dependent yield criteria for sodium silicate glasses – an atomistic simulation approach, Acta Mater. 111 (2016) 129–137.
[4] G. Kermouche, G. Guillonneau, J. Michler, J. Teisseire, E. Barthel, Perfectly plastic flow in silica glass, Acta Mater. 114 (2016) 146–153.
[5] G.L. Peng, Y.H. Wang, A node split method for crack growth problem, Appl. Mech. Mater. 182–183 (2012) 1524–1528.
[6] F. Zhou, J.F. Molinari, Dynamic crack propagation with cohesive elements: a methodology to address mesh dependency, Int. J. Numer. Methods Eng. 59 (1) (2004) 1–24.
[7] N.M. Azevedo, J. Lemos, Hybrid discrete element/finite element method for fracture analysis, Comput. Methods Appl. Mech. Eng. 195 (33–36) (2006) 4579–4593.
[8] N. Moës, J. Dolbow, T. Belytschko, A finite element method for crack growth without remeshing, Int. J. Numer. Methods Eng. 46 (1) (1999) 131–150.
[9] N. Moës, A. Gravouil, T. Belytschko, Non-planar 3D crack growth by the extended finite element and level sets – Part I: mechanical model, Int. J. Numer. Methods Eng. 53 (11) (2002) 2549–2568.
[10] E. Gürses, C. Miehe, A computational framework of three-dimensional configurational-force-driven brittle crack propagation, Comput. Methods Appl. Mech. Eng. 198 (15–16) (2009) 1413–1428.
[11] B. Bourdin, G.A. Francfort, J.-J. Marigo, The Variational Approach to Fracture, Springer, Netherlands, 2008.
[12] C. Miehe, F. Welschinger, M. Hofacker, Thermodynamically consistent phase-field models of fracture: variational principles and multi-field fe implementations, Int. J. Numer. Methods Eng. 83 (10) (2010) 1273–1311.
[13] D. Mumford, J. Shah, Optimal approximations by piecewise smooth functions and associated variational problems, Commun. Pure Appl. Math. 42 (5) (1989) 577–685.
[14] G. Francfort, J.-J. Marigo, Revisiting brittle fracture as an energy minimization problem, J. Mech. Phys. Solids 46 (8) (1998) 1319–1342.
[15] M. Buliga, Energy minimizing brittle crack propagation, J. Elast. 52 (3) (1998) 201.
[16] B. Bourdin, G. Francfort, J.-J. Marigo, Numerical experiments in revisited brittle fracture, J. Mech. Phys. Solids 48 (4) (2000) 797–826.
[17] G. Dal Maso, R. Toader, A model for the quasi-static growth of brittle fractures: existence and approximation results, Arch. Ration. Mech. Anal. 162 (2) (2002) 101–135.
[18] M.A. Msekh, J.M. Sargado, M. Jamshidian, P.M. Areias, T. Rabczuk, Abaqus implementation of phase-field model for brittle fracture, Comput. Mater. Sci. 96 (Part B) (2015) 472–484.
[19] ABAQUS, ABAQUS Documentation, Dassault Systemes, Providence, RI, USA, 2011.
[20] C. Miehe, M. Hofacker, F. Welschinger, A phase field model for rate-independent crack propagation: robust algorithmic implementation based on operator splits, Comput. Methods Appl. Mech. Eng. 199 (45–48) (2010) 2765–2778.
[21] M. Hofacker, C. Miehe, A phase field model of dynamic fracture: robust field updates for the analysis of complex crack patterns, Int. J. Numer. Methods Eng. 93 (3) (2013) 276–301.
[22] C. Miehe, L.-M. Schänzel, Phase field modeling of fracture in rubbery polymers. Part I: finite elasticity coupled with brittle failure, J. Mech. Phys. Solids 65 (2014) 93–113.
[23] N. Singh, C. Verhoosel, R. de Borst, E. van Brummelen, A fracture-controlled path-following technique for phase-field modeling of brittle fracture, Finite Elem. Anal. Des. 113 (2016) 14–29.
[24] C. Miehe, L.-M. Schänzel, H. Ulmer, Phase field modeling of fracture in multi-physics problems. Part I. Balance of crack surface and failure criteria for brittle crack propagation in thermo-elastic solids, Comput. Methods Appl. Mech. Eng. 294 (2015) 449–485.
[25] C. Miehe, M. Hofacker, L.-M. Schänzel, F. Aldakheel, Phase field modeling of fracture in multi-physics problems. Part II. Coupled brittle-to-ductile failure criteria and crack propagation in thermo-elastic-plastic solids, Comput. Methods Appl. Mech. Eng. 294 (2015) 486–522.
[26] C. Miehe, Comparison of two algorithms for the computation of fourth-order isotropic tensor functions, Comput. Struct. 66 (1) (1998) 37–43.
[27] N. Moës, C. Stolz, P.-E. Bernard, N. Chevaugeon, A level set based model for damage growth: the thick level set approach, Int. J. Numer. Methods Eng. 86 (3) (2011) 358–380.
[28] R.O. Ritchie, The conflicts between strength and toughness, Nat. Mater. 10 (11) (2011) 817–822.
[29] C.L. Rountree, S. Prades, D. Bonamy, E. Bouchaud, R. Kalia, C. Guillot, A unified study of crack propagation in amorphous silica: using experiments and simulations, J. Alloy. Compd. 434–435 (2007) 60–63.
[30] H. Choe, D. Chen, J. Schneibel, R. Ritchie, Ambient to high temperature fracture toughness and fatigue-crack propagation behavior in a Mo–12Si–8.5B (at%) intermetallic, Intermetallics 9 (4) (2001) 319–329.
[31] S. Melin, Why do cracks avoid each other?, Int. J. Fract. 23 (1) (1983) 37–45.
[32] Y. Sumi, Z. Wang, A finite-element simulation method for a system of growing cracks in a heterogeneous material, Mech. Mater. 28 (1–4) (1998) 197–206.
[33] T. Bittencourt, P. Wawrzynek, A. Ingraffea, J. Sousa, Quasi-automatic simulation of crack propagation for 2D LEFM problems, Eng. Fract. Mech. 55 (2) (1996) 321–334.
[34] F. Cazes, N. Moës, Comparison of a phase-field model and of a thick level set model for brittle and quasi-brittle fracture, Int. J. Numer. Methods Eng. 103 (2) (2015) 114–143.
[35] G. Molnár, P. Ganster, J. Török, A. Tanguy, Sodium effect on static mechanical behavior of md-modeled sodium silicate glasses, J. Non-Cryst. Solids 440 (2016) 12–25.
[36] M. Mueller, V. Pejchal, G. Žagar, A. Singh, M. Cantoni, A. Mortensen, Fracture toughness testing of nanocrystalline alumina and fused quartz using chevron-notched microbeams, Acta Mater. 86 (2015) 385–395.
[37] C. Miehe, F. Aldakheel, A. Raina, Phase field modeling of ductile fracture at finite strains: a variational gradient-extended plasticity-damage theory, Int. J. Plast. 84 (2016) 1–32.
[38] G. Molnár, M. Ferentzi, Z. Weltsch, G. Szebényi, L. Borbás, I. Bojtár, Fragmentation of wedge loaded tempered structural glass, Glass Struct. Eng. 59 (2016) 1–10.
[39] O. Zienkiewicz, R. Taylor, D. Fox, The Finite Element Method for Solid and Structural Mechanics, 7th ed., Butterworth-Heinemann, Oxford, 2014.